Petroleum Science
https://doi.org/10.1007/s12182-019-00411-2

ORIGINAL PAPER

Simulation on hydrodynamics of non-spherical particulate system using a drag coefficient correlation based on artificial neural network

Sheng-Nan Yan[1,2] · Tian-Yu Wang[1,2] · Tian-Qi Tang[1,2] · An-Xing Ren[1,2] · Yu-Rong He[1,2]

Received: 20 October 2019

Abstract

Fluidization of non-spherical particles is very common in petroleum engineering. Understanding the complex phenomenon of non-spherical particle flow is of great significance. In this paper, coupled with two-fluid model, the drag coefficient correlation based on artificial neural network was applied in the simulations of a bubbling fluidized bed filled with non-spherical particles. The simulation results were compared with the experimental data from the literature. Good agreement between the experimental data and the simulation results reveals that the modified drag model can accurately capture the interaction between the gas phase and solid phase. Then, several cases of different particles, including tetrahedron, cube, and sphere, together with the nylon beads used in the model validation, were employed in the simulations to study the effect of particle shape on the flow behaviors in the bubbling fluidized bed. Particle shape affects the hydrodynamics of non-spherical particles mainly on microscale. This work can be a basis and reference for the utilization of artificial neural network in the investigation of drag coefficient correlation in the dense gas–solid two-phase flow. Moreover, the proposed drag coefficient correlation provides one more option when investigating the hydrodynamics of non-spherical particles in the gas–solid fluidized bed.

Keywords Fluidized bed · Two-fluid model · Drag coefficient correlation · Non-spherical particle · Artificial neural network

List of symbols

C_D	Drag coefficient (dimensionless)
C_x	Fluctuating instantaneous velocity in the lateral direction, m/s
C_y	Fluctuating instantaneous velocity in the vertical direction, m/s
C_z	Fluctuating instantaneous velocity in the depth direction, m/s
$\boldsymbol{D}$	Rate of strain tensor of the solid phase, s^{-1}
d_b	Bubble diameter, m
d_p	Particle diameter, m
e_p	Particle–particle restitution coefficient (dimensionless)
e_w	Particle-wall restitution coefficient (dimensionless)
F_r	Constant in equation for p_s^f, N/m^2
$\mathbf{g}$	Gravitational constant, m/s^2
g_0	Radial distribution function (dimensionless)
$\mathbf{I}$	Unit tensor (dimensionless)
$\boldsymbol{I}_{2D}$	Second invariant of the deviator of the strain rate tensor of solid phase, s^{-2}
p_s	Solid phase pressure, Pa
p_s^f	Solid frictional pressure, Pa
Re	Reynolds number (dimensionless)
$\boldsymbol{u}_g$	Gas velocity, m/s
$\boldsymbol{u}_s$	Solid velocity, m/s
$u_{\mathbf{s,x}}$	Horizontal particle velocity, m/s
$u_{\mathbf{s,y}}$	Vertical particle velocity, m/s
$\boldsymbol{u}_{sp}$	Superficial velocity, m/s
$\boldsymbol{u}_r$	Relative velocity correlation (dimensionless)
$u_{s,\,x,\,RMS}$	Root mean square of horizontal particle velocity, m/s
$u_{s,\,y,\,RMS}$	Root mean square of vertical particle velocity, m/s

Handled by Associate Editor Jun Yao

Edited by Xiu-Qiu Peng

✉ Yu-Rong He
rong@hit.edu.cn

[1] School of Energy Science and Engineering, Harbin Institute of Technology, Harbin 150001, China

[2] Heilongjiang Key Laboratory of New Energy Storage Materials and Processes, School of Energy Science and Engineering, Harbin Institute of Technology, Harbin 150001, China

Published online: 24 December 2019

u'_x Fluctuating hydrodynamic velocity in the lateral directions, m/s
u'_y Fluctuating hydrodynamic velocity in the vertical directions, m/s
u'_z Fluctuating hydrodynamic velocity in the depth directions, m/s

Greek letters

β_{gs} Inter-phase drag coefficient, kg/m^{3}s
β_{Ergun} Drag coefficient calculated by Ergun correlation, kg/m^{3}s
$\beta_{Wen–Yu}$ Drag coefficient calculated by Wen-Yu correlation, kg/m^{3}s
$\gamma_{\theta s}$ Collisional dissipation rate of the granular fluctuating energy, kg/ms^3
ε_g Gas volume fraction (dimensionless)
ε_s Solid volume fraction (dimensionless)
ε_{smax} Solid volume fraction at the maximum packing state (dimensionless)
ε_{smin} Solid volume fraction beyond which frictional force occurs (dimensionless)
θ_s Granular temperature, m^2/s^2
θ_{bubble} Bubble granular temperature, m^2/s^2
$\theta_{particle}$ Particle granular temperature, m^2/s^2
$\kappa_{\theta s}$ Diffusion coefficient, kg/m^{3}s
λ_s Solid bulk viscosity, Pa s
μ_g Gas viscosity, Pa s
μ_s Solid shear viscosity, Pa s
ρ_g Gas density, kg/m^3
ρ_s Solid density, kg/m^3
$\boldsymbol{\tau}_g$ Stress tensor for the gas phase, Pa
$\boldsymbol{\tau}_s$ Stress tensor for the solid phase, Pa
ϕ Sphericity (dimensionless)
ϕ_{gs} Energy exchange between gas phase and solid phase, kg/ms^3
φ_f Internal friction angle of particles, degree
φ_{gs} Blending function (dimensionless)

1 Introduction

In the petroleum industry, multiphase flow (Li et al., 2019; Shi et al. 2019; Yang et al. 2019), heat transfer (Yin et al. 2018), and mass transfer (Zhu et al. 2018) are widely existed. As a typical multiphase flow system, fluidized bed reactor plays a significant role in the development of the petroleum industry (Zhang 2009; Pei et al. 2009), such as fluid catalytic cracking (Wang et al. 2011), coking (Wang et al. 2016), combustion of petroleum coke (Zhang et al. 2012), pyrolysis process (Gao et al. 2013), etc. There are various complex processes in a fluidized bed reactor, involving complicated multiphase flow, heat transfer, and chemical reactions. A deep understanding of the flow behavior and particle transport phenomenon is of pragmatic importance in the optimization and operation of fluidized bed reactor (Yao et al. 2012; Zhao et al. 2018). The particles in fluidization engineering are normally non-spherical and of irregular shapes. Specifically, for the simplicity of research and fast computation, some kinds of non-spherical particles are regarded as the perfectly spherical particles. However, for some occasions, this kind of treatment is not that rigorous and accurate (Das et al. 2018). Non-spherical particles normally suffer more complicated fluid forces, including the shape-induced lift force, the orientation-dependent lift force and drag force (Zhu et al. 2007). Besides, the packing, contacts, and drag force of non-spherical particles are quite different from that of spherical particles (Boyce et al. 2017). He et al. (2018) found that particle shape affects the compaction behavior and compact properties. Compacts of spheroidal particles with larger aspect ratios have larger compressive strength. Consequently, it is necessary to take the influence of particle shape into account in the investigation of fluidization process of non-spherical particles.

Recently, for the simulation work, increasing papers have been published on the numerical simulation of hydrodynamics of non-spherical particles in the gas–solid fluidized beds. Comparatively speaking, more attention has been paid to discrete element method (DEM) (Gan et al. 2017; Breuninger et al. 2019; Han et al. 2015; Chung et al. 2013; Marchelli et al. 2019; Khawaja 2018). Fewer TFM (two-fluid model) works on fluidization behavior of non-spherical particles in gas–solid fluidized bed have been reported. Cardoso et al. (2018) employed TFM to study the hydrodynamics and heat transfer of a biomass gasification process in a pilot-scale bubbling fluidized bed reactor. Biomass particles are mostly located in the middle and upper regions of the bed, while sand particles accumulate at the middle and bottom of the bed. Sharma et al. (2014) modeled the hydrodynamic behavior of biomass particles and biochar particles in a bubbling fluidized bed by TFM. Superficial gas velocity and biomass particle density had significant influence on the mixing/segregation of biomass particles and biochar particles, while the effect of biomass particle diameter was negligible. Hua et al. (2015) conducted a TFM simulation of flow behavior of calcium carbonate in a lab-scale three-dimensional rectangular fluidized bed. It reveals that the drag model with

an assumption of perfectly spherical particles give poor prediction of hydrodynamics of non-spherical particles in a gas–solid fluidized bed. Taking particle sphericity into consideration is necessary when investigating the fluidization of non-spherical particles. Lu et al. (2015) proposed a drag model for non-spherical particles, integrated it into the two-fluid model, and employed it in the simulation of hydrodynamics of non-spherical particles in a supercritical water fluidized bed. The drag model was verified by a comparison between simulation results and experimental data.

For TFM simulations of hydrodynamic behavior of non-spherical particles in gas–solid fluidized beds, a proper and effective drag model is still lacking. Drag model is the key point when simulating the hydrodynamics of non-spherical particulate system. There are two kinds of fluid-particle drag models, which are homogeneous and heterogeneous drag models (Gao et al. 2018). For homogeneous drag models, the particles are assumed to be uniformly distributed in a fluid. Homogenous drag models can be derived from particle-resolved direct numerical simulation (PR-DNS). Heterogeneous drag models can be derived from four approaches: mesoscale-structure-based method, fine grid two-fluid simulation, fine grid CFD–DEM simulation, and particle-resolved DNS simulation. Gao et al. (2018) summarizes eight representative drag models, including three homogeneous drag models: the Gidaspow drag model (Gidaspow 1994), the Beetstra–van der Hoef–Kuipers (BVK) drag model (Beetstra et al. 2007), the (Tenneti–Garg–Subramaniam) TGS drag model (Tenneti et al. 2011), and five heterogeneous drag models: the Sarkar drag model (Sarkar et al. 2016), the Igci drag model (Igci et al. 2011), the Radl drag model (Radl and Sundaresan 2014), the Mehrabadi–Murphy–Subramaniam (MMS) drag model (Mehrabadi et al. 2016), and the energy-minimization multi-scale (EMMS) drag model (Li 1994). Gidaspow drag model consists of the Wen–Yu (Wen 1966) and Ergun equations (Ergun, 1952). Most drag models were derived from simulations and existed drag equations. Moreover, they are validated in one or two fluidization regimes (Gao et al. 2018). Consequently, we want to propose a generalized drag correlation that can be widely applied in different flow regimes. Besides the accuracy, the efficiency is another aspect that should be taken into consideration. As frequently reported, the settling experiments and the wind tunnel experiments are suitable for the conditions of low Reynolds number ($Re \leq 1000$) and high Reynolds number ($Re > 1000$), respectively. In other words, to avoid repeating redundant measurements of drag coefficient is the core point. Time, cost, lab space, and human resource should be used as less as possible. Based on the above-mentioned points, the method of artificial neural network (ANN) comes to our mind. ANN has several outstanding advantages, one of which is the learning ability. In the previous paper (Yan et al. 2019), it has been proved that ANN can well learn and master the complicated rule between the Reynolds number, particle sphericity, and drag coefficient. It is an efficient tool in predicting the drag coefficients of different kinds of shaped particles.

In the approach of TFM, both the fluid phase and solid phase are treated as continuous media and described by Navier–Stokes equations (Miao et al. 2017). TFM can overcome the fatal disadvantage of DEM, which is that the number of calculated particles is substantially restricted when the simulation needs to be finished within practical time using a single personal computer (Sakai et al. 2014). Moreover, TFM can better solve the problem of model scale, computation demand and cost, and efficiency (Rangarajan et al. 2013; Langston et al. 2009). In our previous paper (Yan et al. 2019), a modified Gidaspow-Blend model was established based on the drag coefficient prediction by radial basis neural network (RBFNN). And it was validated in modeling hydrodynamics of non-spherical particles in a gas–solid fluidized bed. In this paper, the modified drag model was further applied in investigating flow behavior of dense gas–solid flow, which is our primary objective. Furthermore, the flow behaviors of the particles with different sphericities were compared. The influence of particle shape on the flow behaviors in the fluidized bed was discussed.

2 Model and numerical settings

2.1 Radial basis neural network

RBFNN is adopted in the prediction of drag coefficient. There are two unique steps for the training process of RBFNN. Generally speaking, the first step adjusts the neuron weights in the hidden layer with a self-organized learning method, which is aiming at allocating the radial basis functions. The second step adjusts the neuron weights in the output layer by the generalized delta rule. Adequate experimental data of drag coefficient for various sphericities with different Reynolds number were collected from the former

researchers' literature. Then, RBFNN was employed to learn the rule between drag coefficient, sphericity, and Reynolds number and predict the drag coefficient for the untested cases with various sphericities and Reynolds number. Then, the authors used the experimental data from the literature and the predicted drag coefficient data to make curve fitting of drag coefficient, sphericity, and Reynolds number. More details can be found in the authors' previous work (Yan et al. 2019).

2.2 CFD model

Two-fluid model is adopted for the simulations of the gas and solid flow in the fluidized bed. This approach considers the solid and gas phases to be continuous and fully penetrating. The two-fluid solver of the open-source code developed by the National Energy Technology Laboratory (NETL), Multiphase Flow with Interphase eXchanges (MFiX) 19.1 release was employed to obtain the solutions of the mass and transport formulas with closure relations by a finite volume method. Governing equations and constitutive relations in Eulerian–Eulerian simulation are shown as follows (Gidaspow 1994).

Conservation of the mass for gas phase and solid phase:

$$\frac{\partial}{\partial t}\left(\varepsilon_{\mathrm{g}}\rho_{\mathrm{g}}\right)+\nabla\cdot\left(\varepsilon_{\mathrm{g}}\rho_{\mathrm{g}}\boldsymbol{u}_{\mathrm{g}}\right)=0 \tag{1}$$

$$\frac{\partial}{\partial t}\left(\varepsilon_{\mathrm{s}}\rho_{\mathrm{s}}\right)+\nabla\cdot\left(\varepsilon_{\mathrm{s}}\rho_{\mathrm{s}}\boldsymbol{u}_{\mathrm{s}}\right)=0 \tag{2}$$

$$\varepsilon_{\mathrm{g}}+\varepsilon_{\mathrm{s}}=1 \tag{3}$$

Conservation of the momentum for gas phase and solid phase:

$$\frac{\partial}{\partial t}\left(\varepsilon_{\mathrm{g}}\rho_{\mathrm{g}}\boldsymbol{u}_{\mathrm{g}}\right)+\nabla\cdot\left(\varepsilon_{\mathrm{g}}\rho_{\mathrm{g}}\boldsymbol{u}_{\mathrm{g}}\boldsymbol{u}_{\mathrm{g}}\right)=-\varepsilon_{\mathrm{g}}\nabla p+\nabla\cdot\boldsymbol{\tau}_{\mathrm{g}}+\varepsilon_{\mathrm{g}}\rho_{\mathrm{g}}\mathbf{g}-\beta_{\mathrm{gs}}\left(\boldsymbol{u}_{\mathrm{g}}-\boldsymbol{u}_{\mathrm{s}}\right) \tag{4}$$

$$\frac{\partial}{\partial t}\left(\varepsilon_{\mathrm{s}}\rho_{\mathrm{s}}\boldsymbol{u}_{\mathrm{s}}\right)+\nabla\cdot\left(\varepsilon_{\mathrm{s}}\rho_{\mathrm{s}}\boldsymbol{u}_{\mathrm{s}}\boldsymbol{u}_{\mathrm{s}}\right)=-\varepsilon_{\mathrm{s}}\nabla p-\nabla p_{\mathrm{s}}+\nabla\cdot\boldsymbol{\tau}_{\mathrm{s}}+\varepsilon_{\mathrm{s}}\rho_{\mathrm{s}}\mathbf{g}-\beta_{\mathrm{gs}}\left(\boldsymbol{u}_{\mathrm{s}}-\boldsymbol{u}_{\mathrm{g}}\right) \tag{5}$$

Stress tensor for gas phase and solid phase:

$$\boldsymbol{\tau}_{\mathrm{g}}=\varepsilon_{\mathrm{g}}\mu_{\mathrm{g}}\left(\nabla\boldsymbol{u}_{\mathrm{g}}+\nabla\boldsymbol{u}_{\mathrm{g}}^{\mathrm{T}}\right)-\frac{2}{3}\varepsilon_{\mathrm{g}}\mu_{\mathrm{g}}\left(\nabla\cdot\boldsymbol{u}_{\mathrm{g}}\right)\mathbf{I} \tag{6}$$

$$\boldsymbol{\tau}_{\mathrm{s}}=\varepsilon_{\mathrm{s}}\mu_{\mathrm{s}}\left(\nabla\boldsymbol{u}_{\mathrm{s}}+\nabla\boldsymbol{u}_{\mathrm{s}}^{\mathrm{T}}\right)+\varepsilon_{\mathrm{s}}\left(\lambda_{\mathrm{s}}-\frac{2}{3}\mu_{\mathrm{s}}\right)\left(\nabla\cdot\boldsymbol{u}_{\mathrm{s}}\right)\mathbf{I} \tag{7}$$

Gidaspow-Blend drag model (Huilin and Gidaspow 2003)

$$\beta_{\mathrm{Ergun}}=\frac{150\varepsilon_{\mathrm{s}}\left(1-\varepsilon_{\mathrm{g}}\right)\mu_{\mathrm{g}}}{\varepsilon_{\mathrm{g}}\left(\phi d_{\mathrm{p}}\right)^{2}}+\frac{1.75\rho_{\mathrm{g}}\varepsilon_{\mathrm{s}}}{\phi d_{\mathrm{p}}}\left|\boldsymbol{u}_{\mathrm{s}}-\boldsymbol{u}_{\mathrm{g}}\right| \tag{8}$$

$$\beta_{\text{Wen-Yu}}=0.75C_{\mathrm{D}}\left(\frac{\rho_{\mathrm{g}}\varepsilon_{\mathrm{g}}\varepsilon_{\mathrm{s}}}{d_{\mathrm{p}}}\right)\left|\boldsymbol{u}_{\mathrm{s}}-\boldsymbol{u}_{\mathrm{g}}\right|\varepsilon_{\mathrm{g}}^{-2.65} \tag{9}$$

$$\varphi_{\mathrm{gs}}=\frac{\arctan\left[150\times1.75\left(0.2-\varepsilon_{\mathrm{s}}\right)\right]}{\pi}+0.5 \tag{10}$$

$$\beta_{\mathrm{gs}}=\left(1-\phi_{\mathrm{gs}}\right)\beta_{\mathrm{Ergun}}+\phi_{\mathrm{gs}}\beta_{\mathrm{Wen-Yu}} \tag{11}$$

Drag coefficient correlation based on artificial neural network (Yan et al. 2019):

$$\lg C_{\mathrm{D}}=A_0+A_1\lg Re+A_2(\lg Re)^2+A_3(\lg Re)^3+A_4(\lg Re)^4 \tag{12}$$

$$\begin{pmatrix}A_0\\A_1\\A_2\\A_3\\A_4\end{pmatrix}=\begin{pmatrix}-18.5047 & 183.2503 & -613.2826 & 966.0357 & -727.4302 & 211.3367\\ -12.8162 & 75.0120 & -163.6044 & 150.0228 & -49.4788 & 0\\ 0.9571 & -7.8929 & 22.3575 & -25.1512 & 9.8015 & 0\\ 0.4725 & -3.0411 & 5.9850 & -4.2176 & 0.8038 & 0\\ -0.0480 & 0.4531 & -1.0986 & 0.9621 & -0.2671 & 0\end{pmatrix}\begin{pmatrix}1\\\phi\\\phi^2\\\phi^3\\\phi^4\\\phi^5\end{pmatrix} \tag{13}$$

Solid phase pressure:

$$p_{\mathrm{s}}=\varepsilon_{\mathrm{s}}\rho_{\mathrm{s}}\theta_{\mathrm{s}}\left[1+2g_0\varepsilon_{\mathrm{s}}\left(1+e_{\mathrm{p}}\right)\right]+p_{\mathrm{s}}^{\mathrm{f}} \tag{14}$$

Solid shear viscosity (Syamlal and Rogers 1993):

$$\mu_s = \frac{10\rho_s d_p\sqrt{\pi\theta_s}}{96\varepsilon_s(1+e_p)g_0}\left[1+\frac{4}{5}g_0\varepsilon_s(1+e_p)\right]^2 + \frac{4}{5}\varepsilon_s\rho_s d_p g_0(1+e_p)\sqrt{\frac{\theta_s}{\pi}} + \mu_s^f \tag{15}$$

Frictional stress model (Johnson et al. 1990):

$$\mu_s^f = \frac{p_s^f \sin\varphi_f}{2\sqrt{I_{2D}}} \tag{16}$$

$$\boldsymbol{I}_{2D} = -\frac{1}{2}\boldsymbol{D}:\boldsymbol{D} \tag{17}$$

$$\boldsymbol{D} = \frac{1}{2}\left(\nabla\boldsymbol{u}_s + \nabla\boldsymbol{u}_s^T\right) - \frac{1}{3}(\nabla\cdot\boldsymbol{u}_s)\mathbf{I} \tag{18}$$

$$p_s^f = \begin{cases} F_r\frac{(\varepsilon_s-\varepsilon_{smin})^m}{(\varepsilon_{smax}-\varepsilon_s)^n} & \varepsilon_s > \varepsilon_{smin} \\ 0 & \varepsilon_s \le \varepsilon_{smin} \end{cases} \tag{19}$$

The constants used in the frictional stress model are set as follows, $F_r = 0.05$ N/m^2, $m = 2$, $n = 5$, $\varepsilon_{smin} = \varepsilon_{smf}$.

Solid bulk viscosity:

$$\lambda_s = \frac{4}{3}\varepsilon_s\rho_s d_p g_0(1+e_p)\sqrt{\frac{\theta_s}{\pi}} \tag{20}$$

Radial distribution function:

$$g_0 = \left[1-\left(\frac{\varepsilon_s}{\varepsilon_{smax}}\right)^{1/3}\right]^{-1} \tag{21}$$

Table 1 Numerical simulation parameters (Nylon beads)

Parameters	Units	Value
Minimum fluidization velocity, u_{mf}	m/s	1.05
Bed height at minimum fluidization, h_{mf}	m	0.173
Void fraction (fluffed)	–	0.42
Particle density ρ_p	kg/m^3	1131
Particle diameter d_p	μm	3256
Sphericity ϕ	–	0.94
Terminal velocity u_t	m/s	9.94
Gas density ρ_g	kg/m^3	1.225
Gas viscosity μ_g	Pa·s	1.8×10^{-5}
Superficial gas velocity u_{sp}	m/s	2.19, 3.28, 4.38
Bed width	m	0.23
Bed height	m	1.22
Bed depth	m	0.075
Grid number	–	15×80×5
Particle–wall coefficient of restitution e_w	–	0.92
Particle–particle coefficient of restitution e_p	–	0.84

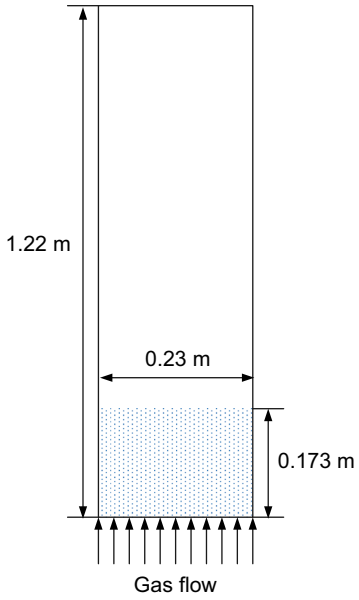

Fig. 1 A 2D schematic diagram of the NETL bubbling fluidized bed (Lungu et al. 2016)

Conservation of the granular fluctuating energy:

$$\frac{3}{2}\left[\frac{\partial}{\partial t}(\varepsilon_s\rho_s\theta_s) + \nabla\cdot(\varepsilon_s\rho_s\boldsymbol{u}_s\theta_s)\right] = \left(-p_s\mathbf{I}+\boldsymbol{\tau}_s\right):\nabla\boldsymbol{u}_s + \nabla\cdot\left(\kappa_{\theta_s}\nabla\theta_s\right) - \gamma_{\theta_s} + \phi_{gs} \tag{22}$$

Collisional dissipation rate of the granular fluctuating energy:

$$\gamma_{\theta s} = \frac{12\left(1-e_p^2\right)g_0}{d_p\sqrt{\pi}}\rho_s\varepsilon_s^2\theta_s^{3/2} \tag{23}$$

2.3 Numerical settings

The bubbling bed is the one that was used in the experiments of NETL, which was mentioned in the work of Lungu et al. (2016). It is a rectangular bed, whose width, depth, and height are 0.23 m, 0.075 m, and 1.22 m, respectively. Figure 2 displays the schematic diagram of the bubbling bed. The relevant parameters and settings employed in the simulation of the fluidized bed are summarized in Table 1. All simulations were run for 40 s. Time-averaged data were obtained with time ranging from 20 to 40 s. A two-dimensional schematic diagram of the setup is shown in Fig. 1. Particles used in this work were nylon beads with a Sauter mean diameter of 3256 μm and density of 1131 kg/m^3. Superficial gas velocities of 2.19 m/s, 3.28 m/s, and

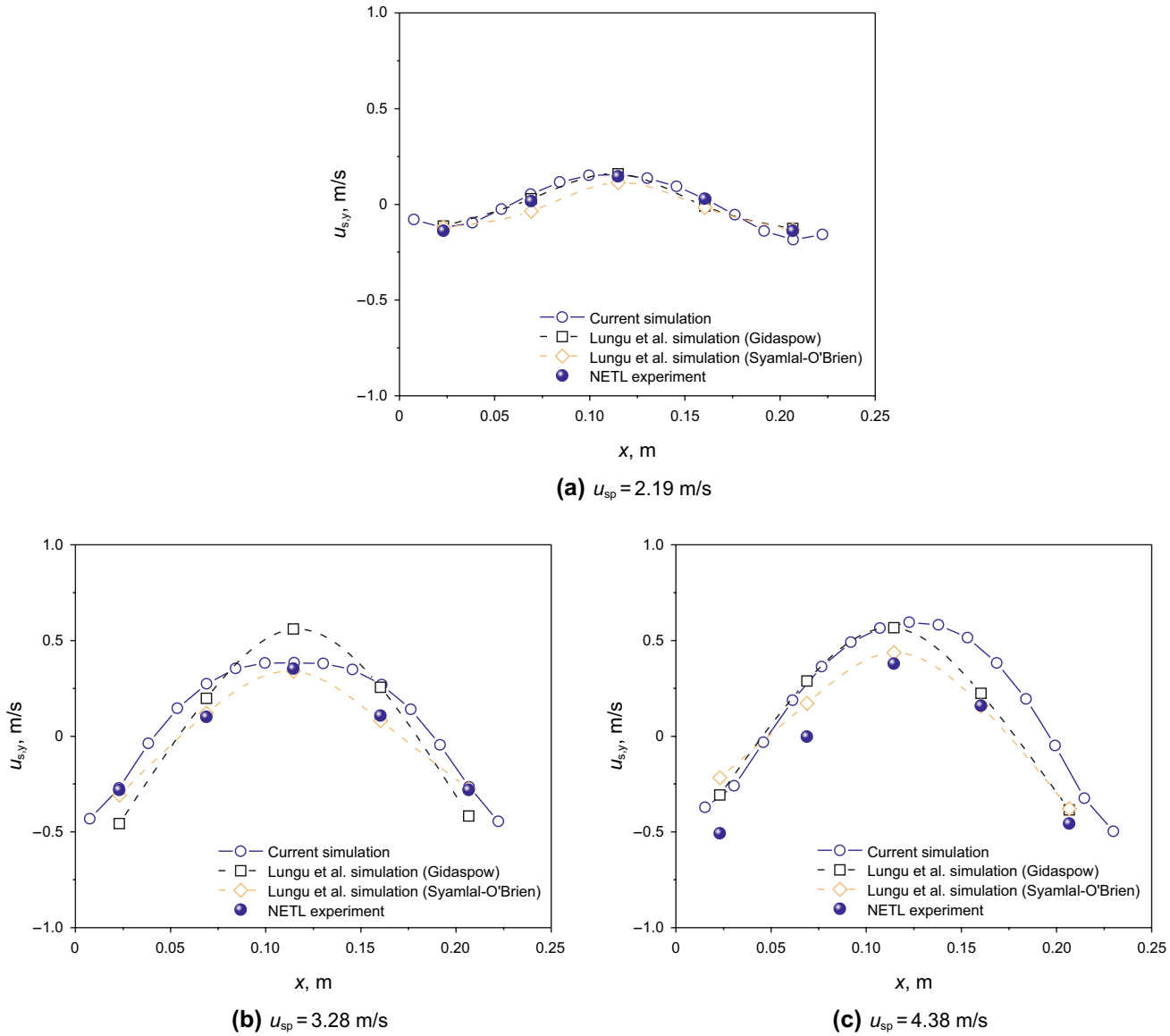

Fig. 2 Vertical particle velocity profiles for various superficial gas velocities at the bed height of 0.0762 m

4.38 m/s approximately correspond to 2, 3, and 4 times of the minimum fluidization velocity, respectively. In the order of above-mentioned superficial gas velocities, the runs fall into case 1, case 2, and case 3, respectively. Particle velocity data were obtained at the bed height of 0.0762 m above the gas distributor. Lateral positions of 0.02356 and 0.20644 m, 0.06928 m, and 0.16072 m, and 0.115 m represent the wall region, annulus region, and center region of the bed, respectively. Such details are exactly the same as the work of Lungu et al. (2016).

For a better prediction and comparison, we performed a 3D simulation. The grid resolution of width (x), depth (y), and height (z) is 15, 5, and 80, respectively. Velocity inlet boundary condition was used at the bed inlet, while a pressure outlet boundary condition was employed at the outlet. Johnson and Jackson boundary conditions were

chosen for the solid phase at the wall, and the gas phase was simulated as no slip. According to work of Altantzis et al. (2015), the suitable specularity coefficient value depends on the superficial gas velocity. Therefore, specularity coefficient of 0.5 was adopted for case 1, and 0.005 for case 2 and case 3. The discretization scheme, superbee, which is recommended by MFiX, was selected to solve the conservation equations. The interphase momentum exchange coefficient between the gas and solid phases is modeled by the correlations of Gidaspow-blend model. The drag coefficient correlation obtained in our previous work is integrated into the model. The numerical parameters are set the same as the experiment.

3 Results and discussions

3.1 Model verification

3.1.1 Particle velocity

The simulation results of particle velocity, flatness factor, and granular temperature were compared with experimental data of NETL. Figure 2 shows the vertical particle velocity profile at the bed height of 0.0762 m above the gas distributor. The proposed drag coefficient correlation describes the interaction between gas phase and solid phase well. Particles move upward in the center and downward near the side walls. With respect to the vertical particle velocity, our simulations perform well for the case with lower superficial gas velocities. For the cases of higher superficial gas velocities, the agreement between the experiments and simulations is not that well. Overall, the variation trend of the experiment is accurately reproduced by our simulations.

3.1.2 Flatness factor (FF)

Wavelet decomposition has been proved to be a useful tool of extracting different frequency ranges while retaining the timestamp of signals. It can be used to classify the fluidized-bed measurement data into noise (microscale), flow structures like clusters or bubbles (mesoscale), and equipment (macroscale) (Chew et al. 2012). Wavelet analysis, which is an important time–frequency domain analysis tool for multi-resolution analysis, can be employed to decompose the time series into sub-signals of different levels (i.e., frequency bands) and keep the dynamic characteristics (Wu et al. 2018). At the first scale of decomposition (Scale 1), N Hz signal is divided into the first scale of approximation (A_1) and the first scale of detail (D_1), whereby A_1 contains the lower half of the frequency range and D_1 contains the higher half. The signals of A_1 and D_1 reconstruct the original signal. This is a reversed wavelet decomposition.

$$x = D_1 + D_2 + D_3 + \cdots + D_j + A_j \tag{24}$$

From scale j to scale $j+1$, each approximation A_j is further decomposed into low-frequency A_{j+1} and high-frequency D_{j+1} signals.

$$D_j : [2^{-(j+1)}f_s, 2^{-(j)}f_s] \tag{25}$$

$$A_j : [0, 2^{-(j+1)}f_s] \tag{26}$$

Flatness factor (FF) is the normalized fourth-order statistical moment, which is calculated by the detail coefficients of axial fluctuating velocity signal. It characterizes the intermittent nature of the flow. The expression is shown below, in which $<\cdot>$ indicates the arithmetic average over N. Based on fluctuation velocity, flatness factor of 3 means that there is no intermittence and particle fluctuation velocity is in Gaussian distribution. Flatness factor smaller than 3 represents the strong periodicity of particle fluctuation velocity. Flatness factor larger than 3 shows the strong intermittence caused by coherent structures (Sun et al. 2011). Flatness factor is a parameter that characterizes the turbulence of the flow. The formula of flatness factor is shown as follows (Sun et al. 2011).

$$FF_j = \frac{\left\langle \left[D_j(i)\right]^4 \right\rangle_N}{\left\langle \left[D_j(i)\right]^2 \right\rangle_N^2} \tag{27}$$

Figure 3 shows the comparisons of predicted FF and experimental FF at regions of the wall, annulus, and bed center. FF decreases in the direction of walls to the center. At the walls, our simulation fails to reproduce the FF information at scale D_1 to D_2. Overall, our simulations capture the FF variation trend of the non-spherical particles in the bubbling fluidized bed reasonably.

3.1.3 Bubble granular temperature

Granular temperature is of great significance in the flow, mixing, segregation, and attrition phenomena of the particulate systems and associated theories (Biggs et al. 2008).

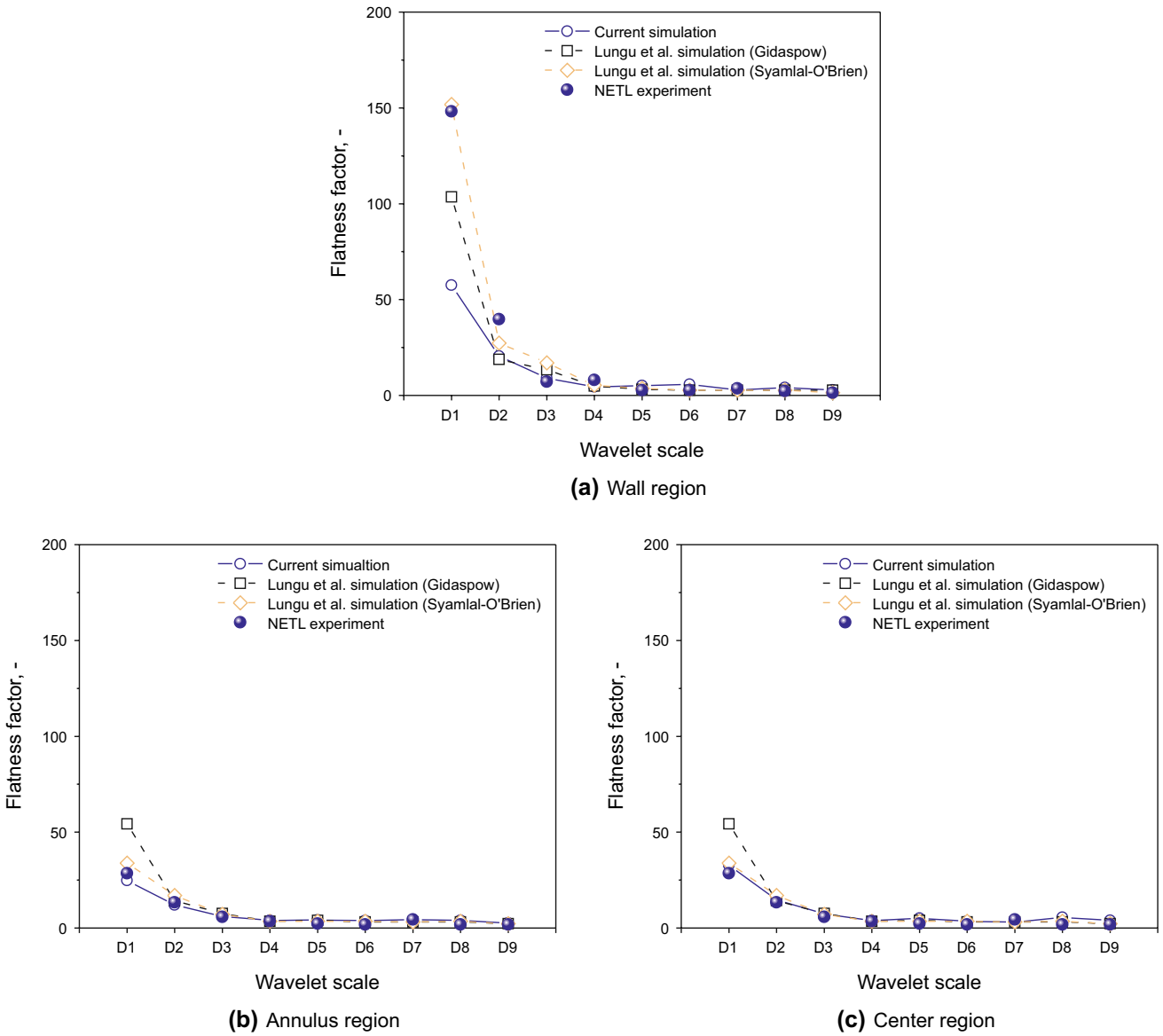

Fig. 3 Predicted and measured axial fluctuating particle velocity flatness factors at three different lateral regions (u_{sp} = 2.19 m/s)

There are two kinds of granular temperature in fluidized beds, namely particle granular temperature and bubble granular temperature. Particle granular temperature, known as the classical granular temperature, can be directly obtained via solving the granular temperature equations in the CFD codes. The particle granular temperature is 2/3 of the random particle kinetic energy. It originates from the oscillation of particles in small regions for a small time period and varies with time and position. The particle granular temperature, which is associated with the particle velocity fluctuation, is proportional to the mean square of the random motion of particles. The intensity of the particle velocity fluctuations defines the stresses, viscosity, and pressure of the solid phase (Gidaspow 1994). It can be calculated as follows.

$$\theta_{\text{particle}} = \frac{1}{3}\left[\langle C_x C_x\rangle + \left\langle C_y C_y\right\rangle + \left\langle C_z C_z\right\rangle\right] \tag{28}$$

Bubble granular temperature (Jung et al. 2005) can be calculated from the normal Reynolds stresses per unit bulk density (Gidaspow and Bacelos 2018):

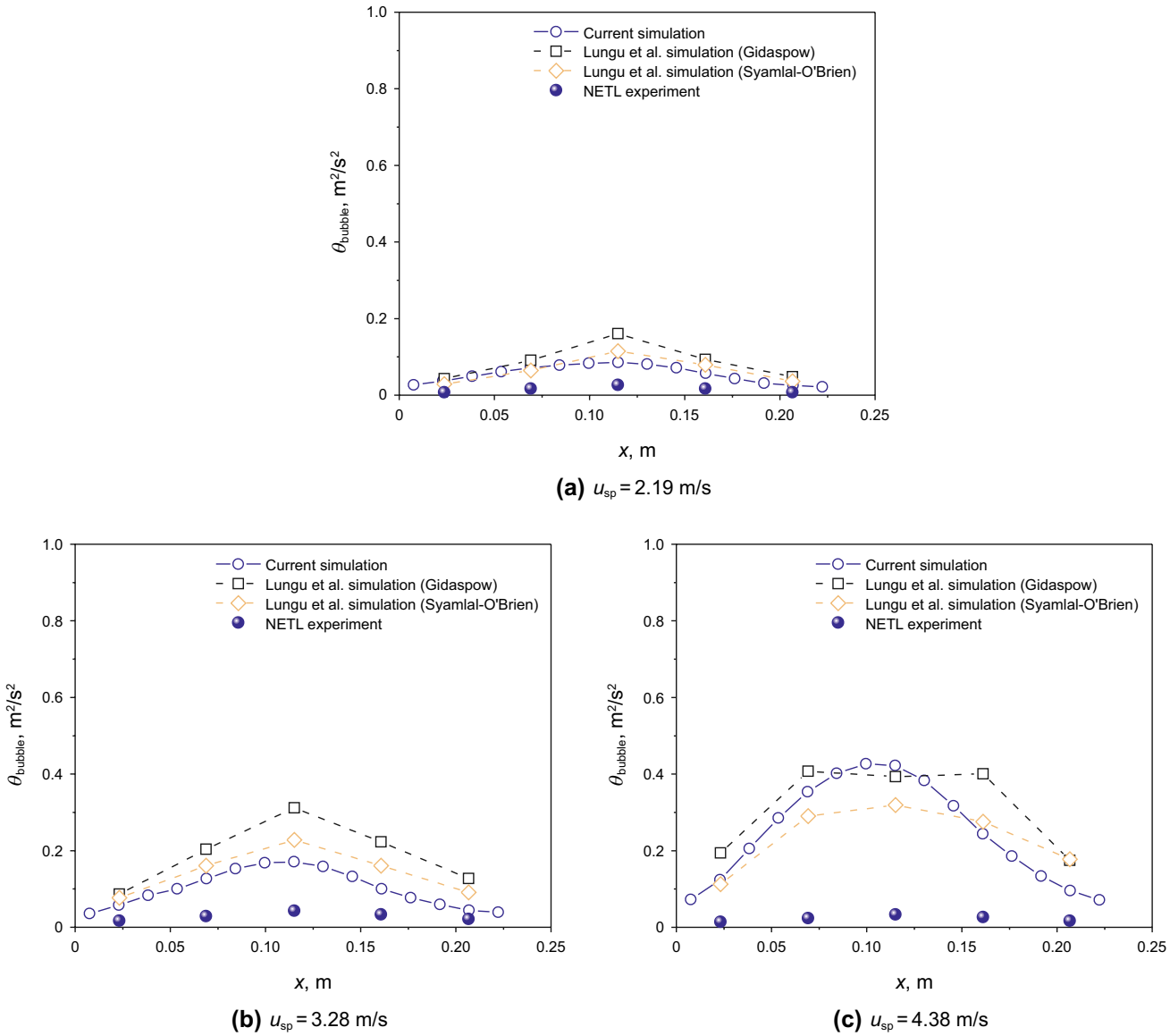

Fig. 4 Bubble granular temperature profiles at the bed height of 0.0762 m for different superficial velocities

$$\theta_{\text{bubble}} = \frac{1}{3}\left[\overline{u'_x u'_x} + \overline{u'_y u'_y} + \overline{u'_z u'_z}\right] \tag{29}$$

Figure 4 shows the profiles of bubble granular temperature. Normally the bubble granular temperature is almost an order of magnitude larger than the particle granular temperature. This is due to the motion of bubbles in the fluidized bed. For the simulation results, the superficial gas velocity has a strong influence on the bubble granular temperature. For case 1, the authors' simulation results are closer to the experimental data. With respect to case 2 and case 3, simulation results have a relatively large deviation from the experimental data, but similar with the results of Lungu et al. (Lungu et al. 2016). In the simulation, the velocity fluctuation increases with the increasing superficial gas velocity. Thus, the bubble granular temperature is larger at higher superficial gas velocity. In the experiments, the bubble granular temperature values change only a little at various superficial gas velocities. This is the reason that the simulation fails to reproduce the bubble granular temperature profile at higher superficial gas velocities.

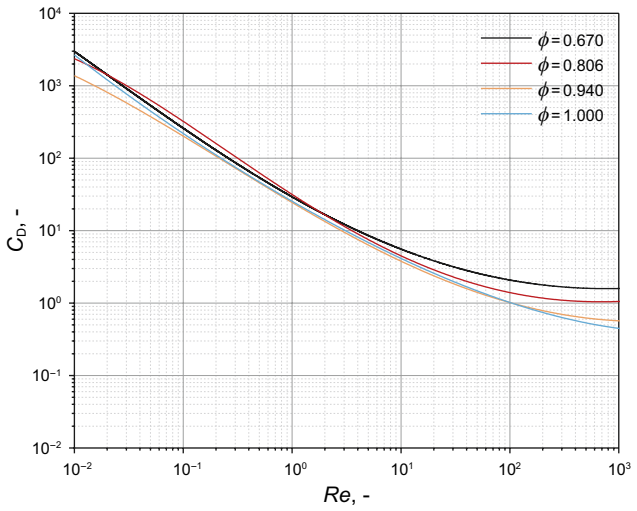

Fig. 5 Drag coefficient comparison for particles with various sphericities

3.2 Particle shape effect

In this section, a series of simulations for different shaped particles were conducted. Besides, the nylon beads in the work of Lungu et al. (2016), three kinds of particles, including tetrahedron, cube, and sphere, are employed in the simulation. Particles' shape effect on the flow behaviors in the fluidized bed was further studied and discussed. The particle velocity, granular temperature, and flatness factor distribution were mainly investigated and analyzed.

3.2.1 Drag coefficient comparison

To compare the difference between the four kinds of particles, the curves for drag coefficient and Reynolds number are drawn in Fig. 5. In the current simulation, the particle Reynolds number ranges from 100 to 400. It can be clearly seen that the drag coefficient has a big difference when the particle Reynolds number is beyond 100. In the following sections, it will be shown that the difference of drag coefficient has an influence on some parameters.

3.2.2 Bubble properties

Figure 6 shows the instantaneous bubble snapshot. To better illustrate the bubble growth process for fluidized bed filled with non-spherical particles, the bubble snapshot at different instants is only presented for the case of sphericity 0.670, which deviates from spherical particles most. The bubble forms at the bottom of the bed. With the upward gas, the bubble size gradually increases. When the bubble reaches to the top of the bed, the bubble begins to break up. It denotes that the bubble growth process in non-spherical particulate system is similar with the well-known bubble growth process in bubbling fluidized beds.

3.2.3 Particle velocity

Figure 7a shows the horizontal particle velocity variation with different particle sphericities. Particle velocity data were chosen from those at the bed height of 0.0762 m. Particle sphericity has a weak influence on the horizontal particle velocity. The profiles of the horizontal particle velocity for four cases are almost the same. In the left part of the bed, particles move toward the right. In the right part of the bed, the trend is just the opposite. Figure 7b shows the vertical particle velocity profiles under different particle sphericities. The trend for four cases is similar. Particles move upward in the core and annulus region and downward near the walls.

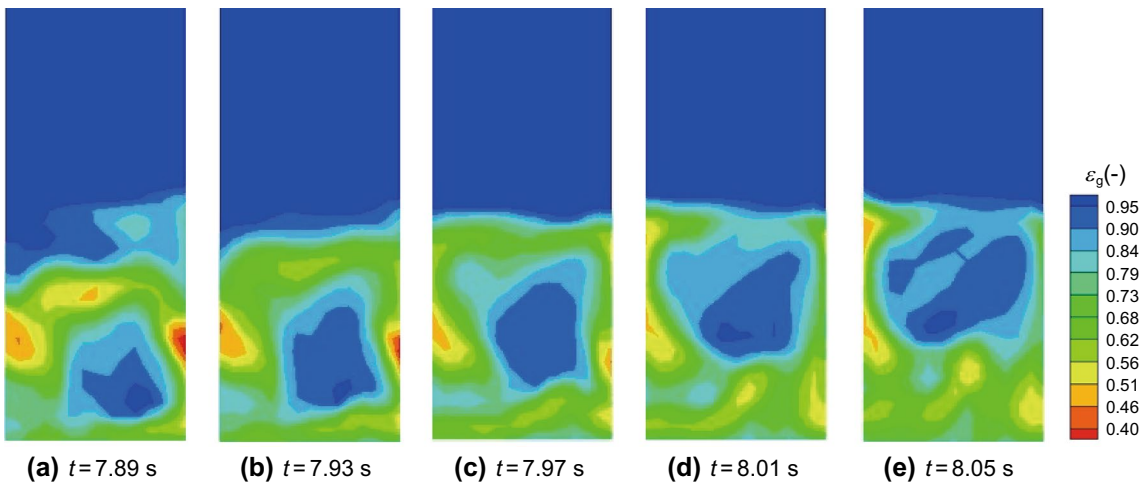

Fig. 6 Instantaneous snapshots of bubbles in the bed ($\phi = 0.670$)

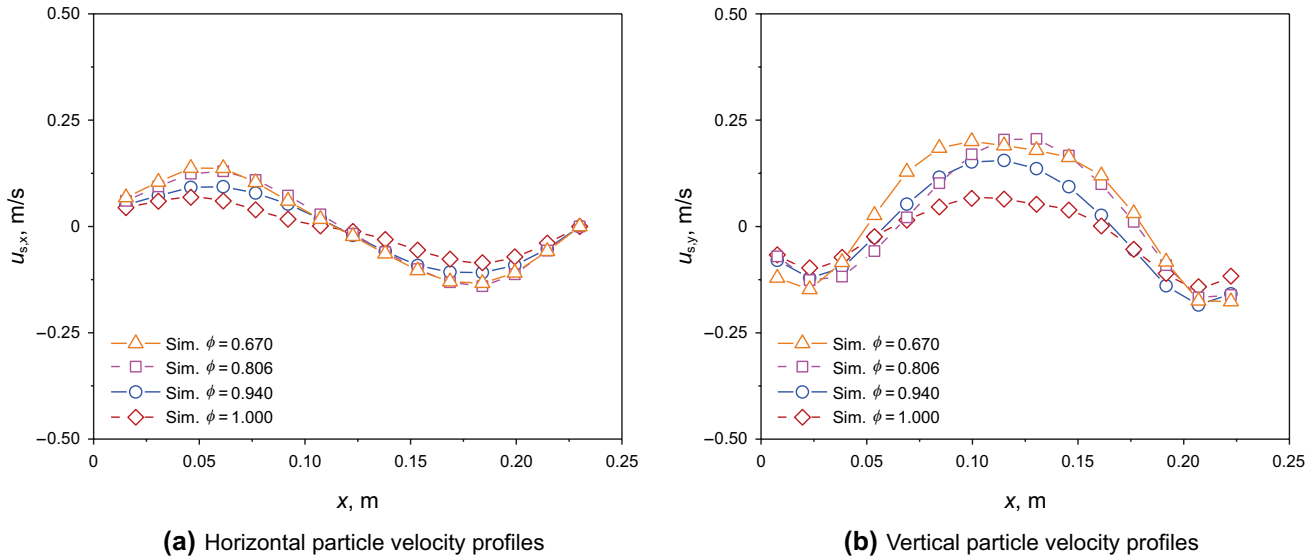

Fig. 7 Particle velocity profiles at the bed height of 0.0762 m

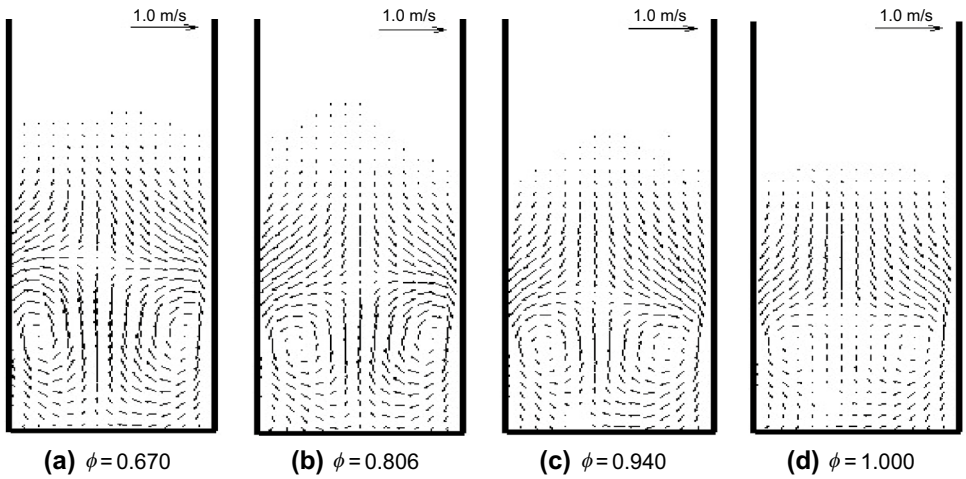

Fig. 8 Time-averaged particle velocity vector profiles

Obviously, particle sphericity influences the vertical particle velocity. The lower the particle sphericity, the higher the vertical particle velocity. If the other conditions are the same and only the particle sphericities are different, the particles with a lower sphericity have a larger drag force that acts on them. Hence, the vertical particle velocity of particles with lower sphericities is higher.

Figure 8 presents the time-averaged particle velocity vector distribution. It can be found that the particle movement trend for the four cases is very similar. The particles move upward through the central region of the bubbling fluidized bed. After the particles reach the top of the bed, they begin to move downward the side walls. The magnitude of the particle velocity for the cases of sphericity of 0.670 and 0.806 is larger than the cases with higher sphericities of

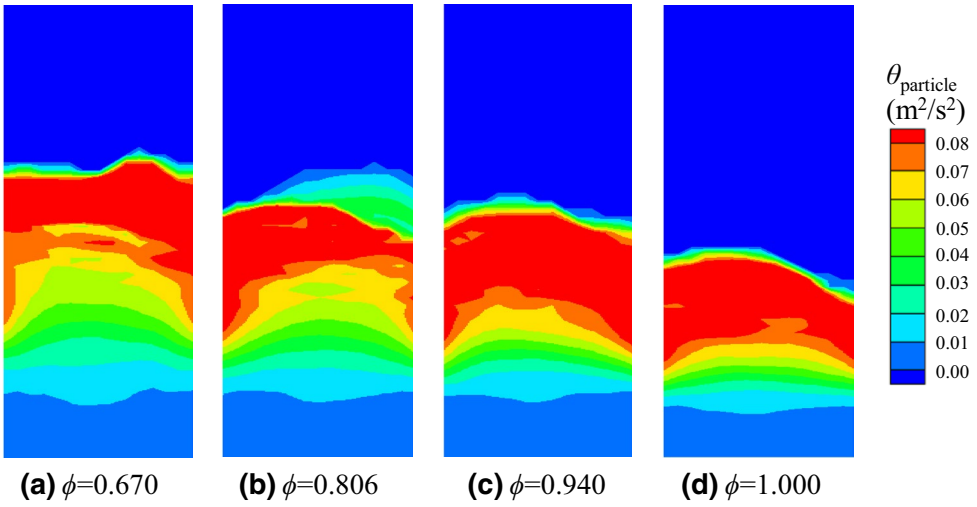

Fig. 9 Time-averaged particle granular temperature profiles

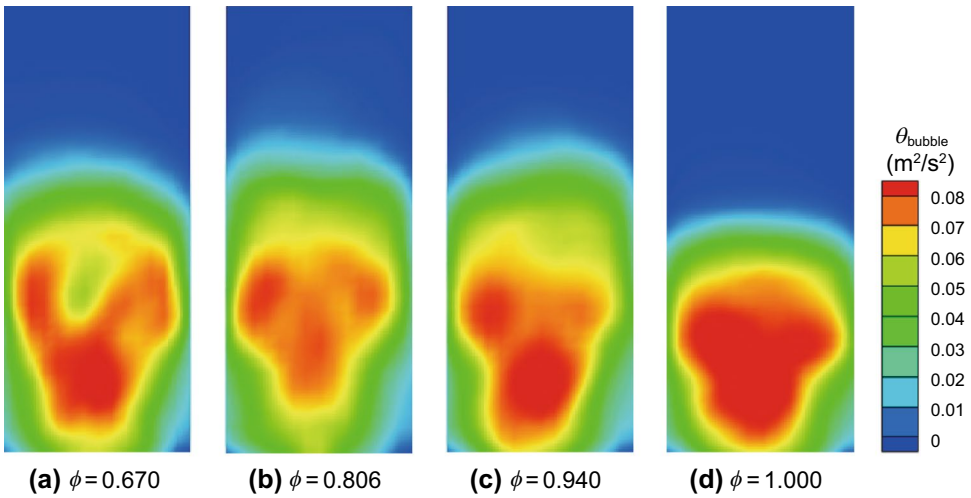

Fig. 10 Time-averaged bubble granular temperature snapshot

0.940 and 1.000. It is demonstrated that the particles with smaller sphericity have larger particle velocity. The maximum bed height can be determined from the particle vector plots. It is also found that the particle sphericity slightly affects the maximum bed height. The maximum bed height nearly decreases with the increase in the particle sphericity.

3.2.4 Granular temperature

Figure 9 shows the profiles of time-averaged particle granular temperature. It is shown that the particles move more violently on the top of the bed. With regards to the central region and bottom region of the bed, the particles movement is a little weaker. It can be clearly seen that the bed expansion decreases with increasing sphericity. Particles with smaller sphericities have larger drag force. Thus, the interaction between gas phase and solid phase is more strengthened for particles with smaller sphericities, which leads to a larger bed expansion.

Figure 10 shows the time-averaged bubble granular temperature distribution. For all cases, the bubble granular temperature in the central region is higher than other

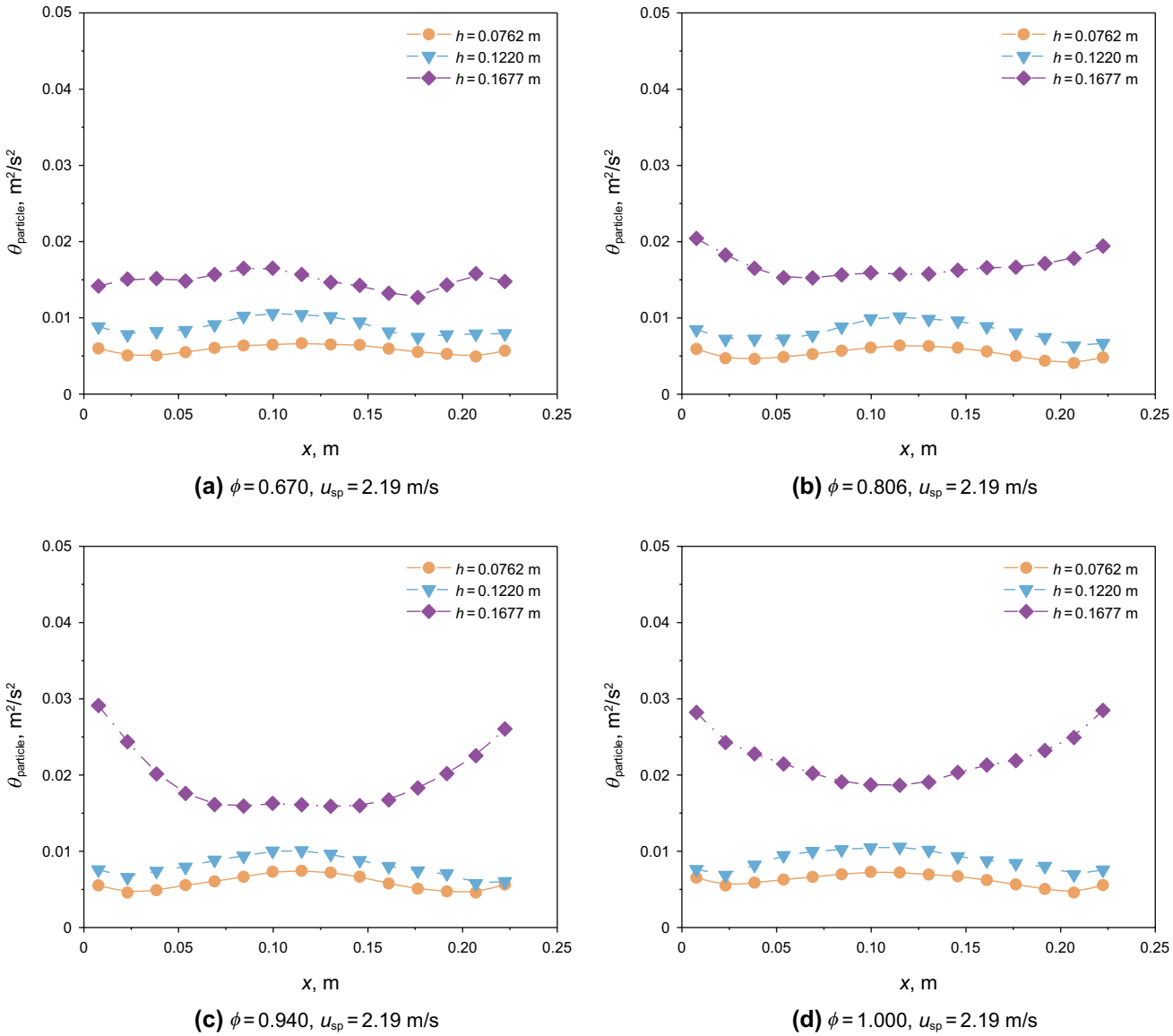

Fig. 11 Particle granular temperature distribution along different bed heights (u_{sp} = 2.19 m/s)

regions. Compared with Fig. 9, it is found that the bubble granular temperature is higher than the particle granular temperature in the central region and at the bottom of the bed, while at the top of the bed, the particle granular temperature is higher than the bubble granular temperature. On the top of the bed, the random oscillations of individual particles play a major role. In the central region and at the bottom of the bed, the motion of bubbles is more predominant. The essence of the different distributions of two kinds of granular temperature is the different types of particles movement.

Figure 11 shows the particle granular temperature distribution at three different bed heights, which correspond to the bottom region, central region, and top region. The particle granular temperature increases with the increase in the bed height. Particles move more violently at the top of the bed. For the case with the particle sphericity of 0.670, the particle granular temperature at the top of the bed is the smallest, compared with three other cases at the same bed height. With respect to all the four cases, the particle granular temperature at the bottom region and central region are

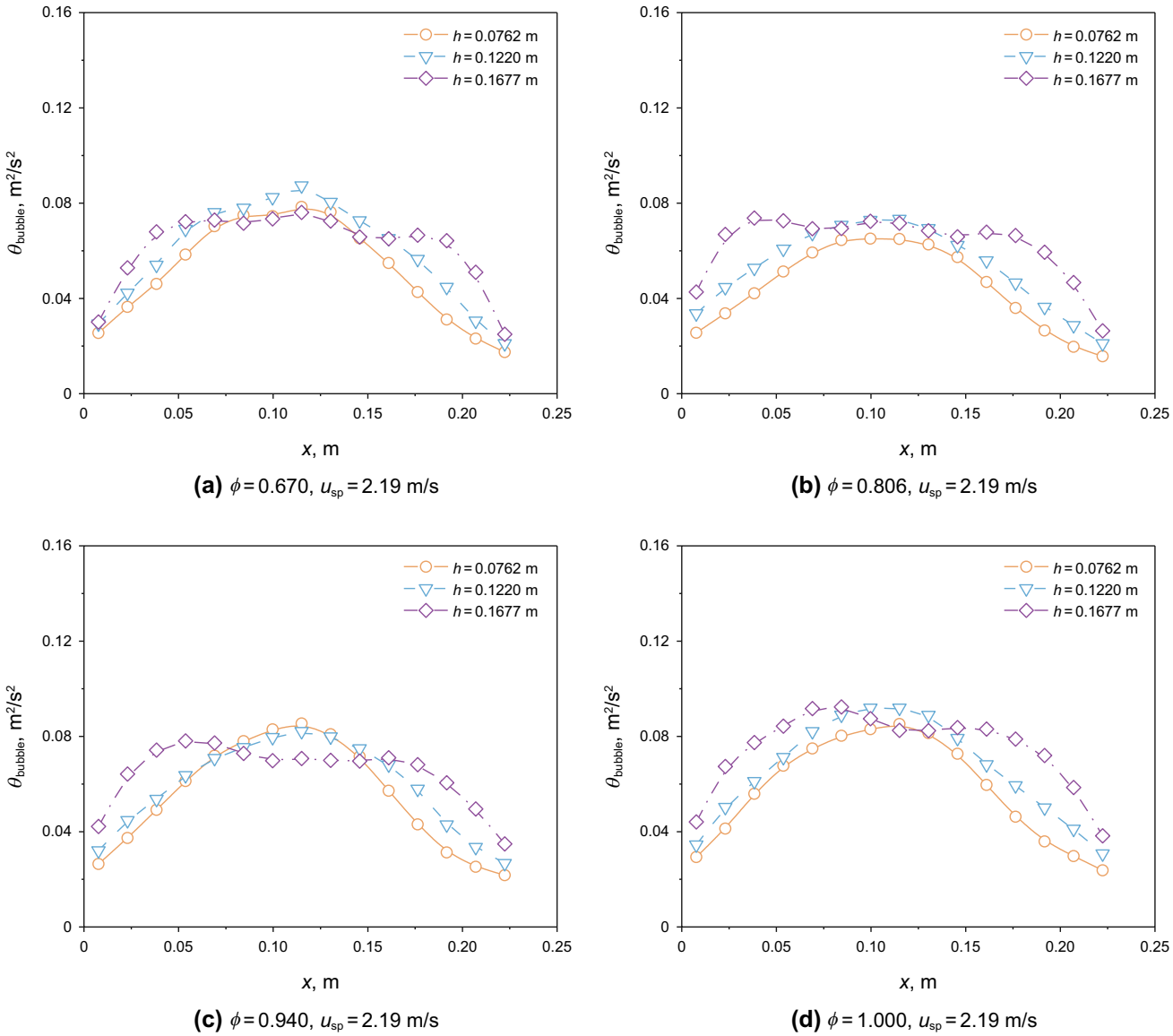

Fig. 12 Bubble granular temperature distribution along different bed heights (u_{sp} = 2.19 m/s)

similar, respectively. However, particles with larger sphericities have larger particle granular temperature on the top of the bed.

Figure 12 displays the bubble granular temperature profiles at three different bed heights. For all the four cases, the variation trend is similar. At the top region of the bed, the bubble granular temperature is lower in the center than that of the annulus region and wall region. The bubble granular temperature is approximately larger for the central region than that of the bottom region. The bubble granular temperature profiles for the four cases are quite similar. It can be concluded that particle shape hardly changes the magnitude of bubble granular temperature at different bed heights. The bubble granular temperature, which is a parameter on the mesoscale level, is less influenced by the particle shape. This can be well illustrated in Sect. 3.2.6.

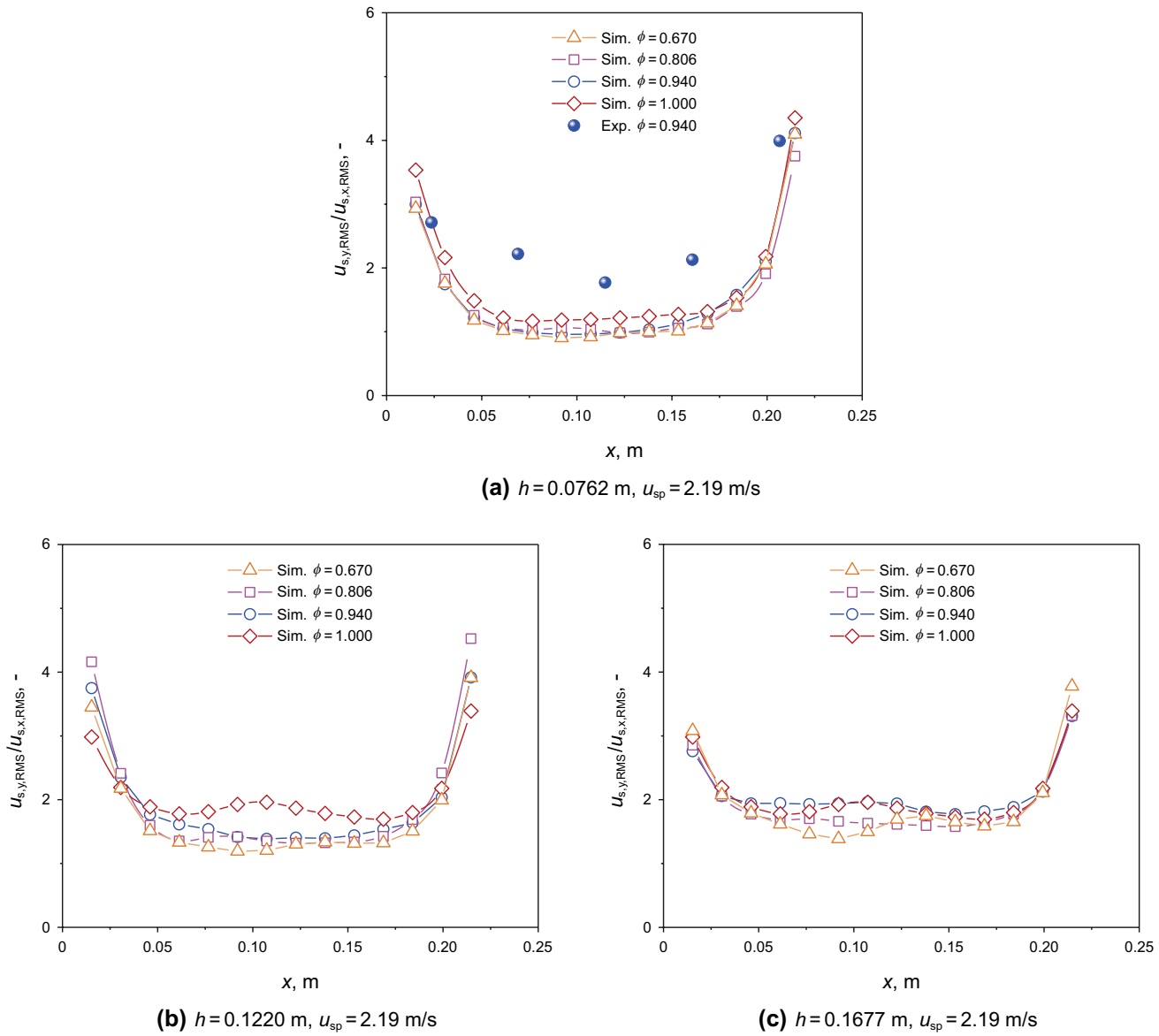

Fig. 13 System isotropy based on particle velocity RMS at different bed heights

3.2.5 RMS distribution

The root mean square (RMS) distribution characterizes the random and fluctuating behavior of the particle velocities. The isotropy of the system is quantified by the ratios of the vertical and horizontal RMS, $u_{s,\,y,\,RMS}/u_{s,\,x,\,RMS}$. The ratio of 1 indicates the system behaves the most isotropic. The RMS velocity is the RMS difference between the instantaneous velocity and mean velocity. It is shown as follows.(Lungu et al. 2016)

$$\frac{u_{s,\,y,\,RMS}}{u_{s,\,x,\,RMS}} = \frac{\sqrt{\frac{1}{N-1}\sum_{n=1}^{N}\left(u_{s,\,y}(n) - \overline{u_{s,\,y}}\right)^2}}{\sqrt{\frac{1}{N-1}\sum_{n=1}^{N}\left(u_{s,\,x}(n) - \overline{u_{s,\,x}}\right)^2}} \tag{30}$$

Figure 13 presents the RMS distribution for the four kinds of particles at three different bed heights. Because of the appearance of the bubbles, the isotropy of the flow is strengthened in the central region at the bottom region and the central region. On the top region of the bed, the

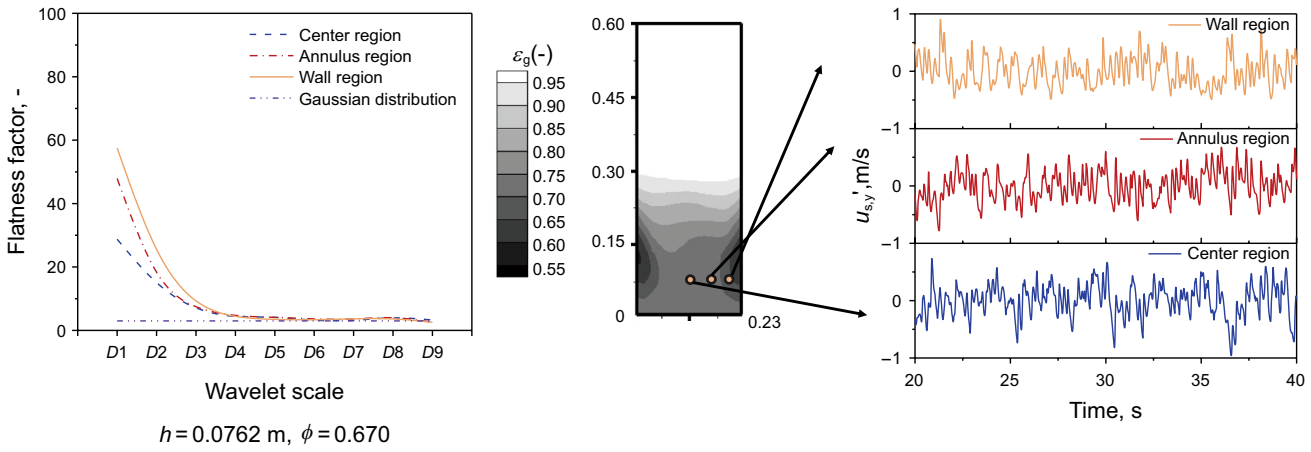

Fig. 14 Distribution of particle fluctuation velocity flatness factor at bed height of 0.0762 m ($\phi = 0.670$)

anisotropy of the flow is weakened at the walls. For each bed height, the difference of the RMS distribution for four kinds of particles is small. It denotes that particle sphericity has a minor effect on the particle fluctuation.

3.2.6 Flatness factor distribution

In essence, a fluidization process is multi-scale. It is consisted of microscale characterized by individual particle size, mesoscale corresponding to bubbling size of cluster size, and macroscale linked with the size of reactor or unit (Yang and Leu 2009). Figure 14 shows the flatness factor distribution in different regions of the bubbling fluidized bed. From the wall to the center, the fluctuation velocity gradually increases. It is because that bubbles mainly appear in the center and annulus region. The mean free path of particles is longer in the center and annulus region. The flatness factor decreases from wall region to center region, which shows an opposite trend compared with the fluctuation velocity. According to the work of Lungu et al. (2016), D_1–D_3 represents the microscale, D_4–D_8 represents the mesoscale, and D_9 represents the macroscale, which can be validated by the flatness factor profiles at different detail signals. For all the three regions, flatness factor is close to Gaussian distribution in the range of D_4–D_9, which denotes the large-scale and low-frequency structures are stable and in order. From D_1–D_3, the flatness factor is much greater than 3, demonstrating the strong intermittency of the flow. In each region, the four flatness factor curves differ from each other in the range of D_1–D_3 and get closer from D_4 to D_9. The gas–solid two-phase flow is more intermittent close to the wall, which reveals the anisotropy of the flow. In the wall region, the particle concentration is denser, and particle–particle collision and particle–wall collision coexist, leading to more energy dissipation via momentum transfer. In the annulus region and center region, the bubbles, which are of mesoscale, are the major movement form of particles. Compared with the wall region, the flow in this region is more isotropic.

Figure 15 displays the flatness factor profiles for the annulus region at various bed heights. The flatness factor for four cases deviates from each other ranging from D_1–D_3. From D_4–D_9, the distribution for three bed heights is similar and close to Gaussian distribution. The flatness factor decreases in the range of D_1–D_3. The flatness factor gets much closer from D_4–D_9 and closer to the Gaussian distribution. The difference of particle shape largely changes the flatness factor for the microscale structure and hardly alters that for the mesoscale structure and macroscale structure. It is found that particle shape influences the microscale structure a lot and has a minor effect on the mesoscale structure and macroscale structure.

4 Conclusions

In this paper, a couple of simulations were conducted using Eulerian–Eulerian approach with closures from the KTGF. Simulation results were compared with the corresponding NETL experimental data and Lungu et al. (2016)'s simulation results. The modified Gidaspow-blend drag model, which is based on the drag coefficient correlation obtained from artificial neural network in our previous paper, was

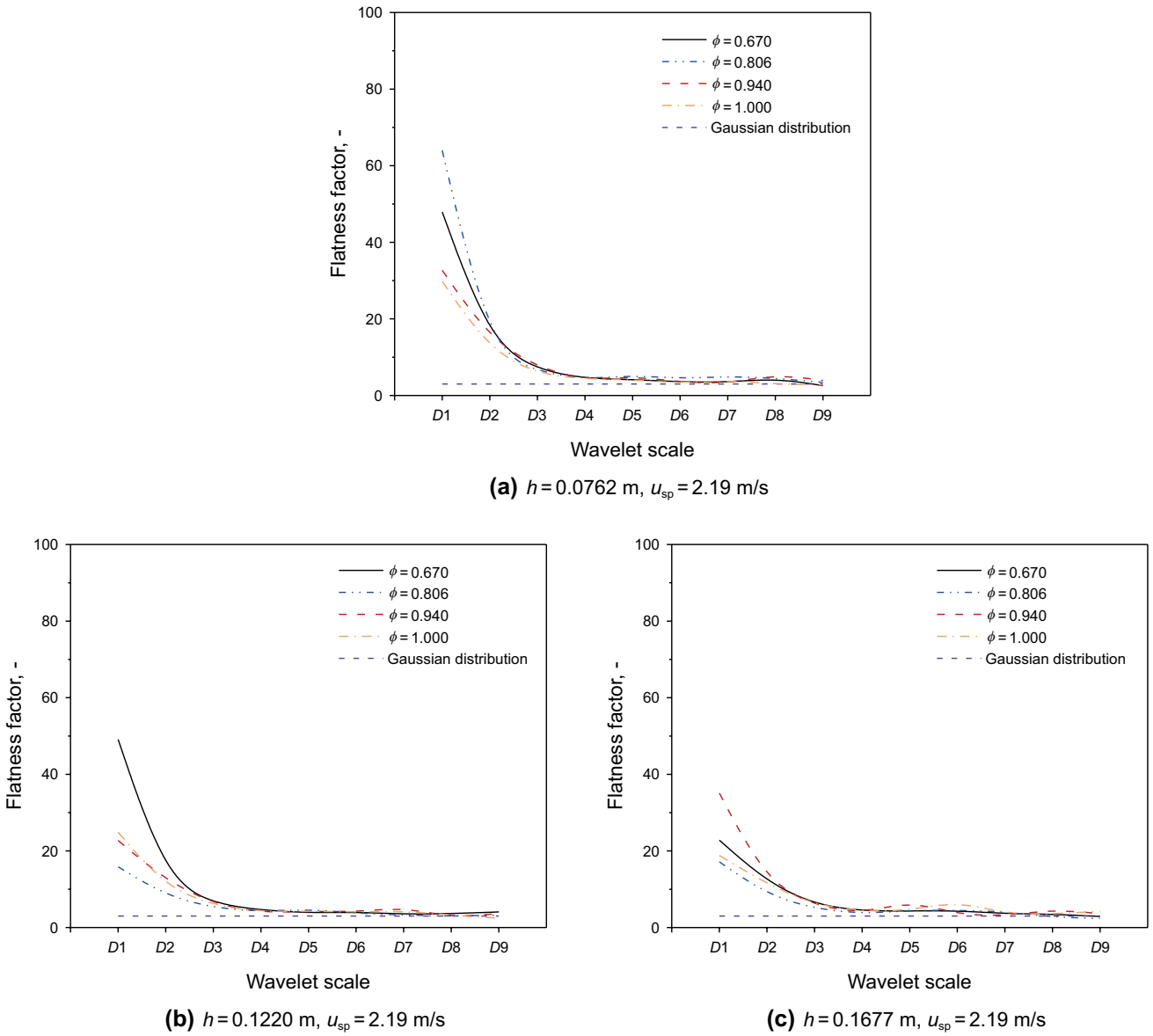

Fig. 15 Flatness factor distribution at different bed heights (u_{sp} = 2.19 m/s)

employed in the simulations; simulation results agree well with the experimental data. Moreover, the effect of particle shape on the flow behavior of particles in bubbling fluidized bed was investigated.

The main conclusions can be drawn as follows:

(1) Two-fluid model, which is coupled with the modified drag model based on the drag coefficient obtained from the RBFNN method, can reasonably predict the flow behavior of non-spherical particles.

(2) Particles with lower sphericities have larger vertical particle velocity. The particle shape has a weak influence on the random and fluctuating behavior of the particle velocities. In the fluidized bed, the particles move more violently on the top of the bed, but move weakly at the center and the bottom of the bed. The lower the particle sphericity is, the larger the bed expansion is.

(3) Particle shape can change the velocity distribution and particle granular temperature distribution, which is on the particle-scale level. Particle shape has a strong influence on the flatness factor distribution in the microscale structure and a minor influence in the mesoscale structure and macroscale structure.

This work can be a reference for the application of the drag coefficient correlation in the fluidization process of non-spherical particles. The modified drag model can facilitate the simulation of complex process of multiphase flow in the process of petroleum engineering. Theoretically, the proposed drag coefficient correlation can be applied to the entire range of Reynolds number. However, it needs to be further validated under different Reynolds number and sphericities, which will be conducted in our future work.

Acknowledgements The authors gratefully acknowledge the financial support by the National Natural Science Foundation of China (Grant No. 51706055).

References

Altantzis C, Bates RB, Ghoniem AF. 3D Eulerian modeling of thin rectangular gas–solid fluidized beds: estimation of the specularity coefficient and its effects on bubbling dynamics and circulation times. Powder Technol. 2015;270:256–70. https://doi.org/10.1016/j.powtec.2014.10.029.

Beetstra R, van der Hoef MA, Kuipers JAM. Drag force of intermediate Reynolds number flow past mono- and bidisperse arrays of spheres. AIChE J. 2007;53(2):489–501. https://doi.org/10.1002/aic.11065.

Biggs M, Glass D, Xie L, Zivkovic V, Buts A, Curt Kounders MA. Granular temperature in a gas fluidized bed. Granul Matter. 2008;10(2):63–73. https://doi.org/10.1007/s10035-007-0077-8.

Boyce C, Ozel A, Rice N, Rubinstein G, Holland D, Sundaresan S. Effective particle diameters for simulating fluidization of non-spherical particles: CFD–DEM models versus MRI measurements. AIChE J. 2017;63(7):2555–68. https://doi.org/10.1002/aic.15623.

Breuninger P, Weis D, Behrendt I, Grohn P, Krull F, Antonyuk S. CFD–DEM simulation of fine particles in a spouted bed apparatus with a Wurster tube. Particuology. 2019;42:114–25. https://doi.org/10.1016/j.partic.2018.03.015.

Cardoso J, Silva V, Eusébio D, Brito P, Tarelho L. Improved numerical approaches to predict hydrodynamics in a pilot-scale bubbling fluidized bed biomass reactor: a numerical study with experimental validation. Energy Convers Manag. 2018;156:53–67. https://doi.org/10.1016/j.enconman.2017.11.005.

Chew J, Hays R, Findlay J, Knowlton T, Karri S, Cocco R, Hrenya C. Cluster characteristics of Geldart Group B particles in a pilot-scale CFB riser I. Monodisperse systems. Chem Eng Sci. 2012;68(1):72–81. https://doi.org/10.1016/j.ces.2011.09.012.

Chung Y, Liao H, Hsiau S. Convection behavior of non-spherical particles in a vibrating bed: discrete element modeling and experimental validation. Powder Technol. 2013;237:53–66. https://doi.org/10.1016/j.powtec.2012.12.052.

Das S, Deen NG, Kuipers JAM. Multiscale modeling of fixed-bed reactors with porous (open-cell foam) non-spherical particles: hydrodynamics. Chem Eng J. 2018;334:741–59. https://doi.org/10.1016/j.cej.2017.10.047.

Ergun S. Fluid flow through packed columns. Chem Eng Prog. 1952;48:89–94.

Gan J, Zhou Z, Yu A. Micromechanical analysis of flow behaviour of fine ellipsoids in gas fluidization. Chem Eng Sci. 2017;163:11–26. https://doi.org/10.1016/j.ces.2017.01.020.

Gao J, Xu T, Wang G, Zhang A, Xu C. Reaction behavior of oil sand in fluidized-bed pyrolysis. Pet Sci. 2013;10(4):562–70. https://doi.org/10.1007/s12182-013-0307-0.

Gao X, Li T, Sarkar A, Lu L, Rogers W. Development and validation of an enhanced filtered drag model for simulating gas–solid fluidization of Geldart A particles in all flow regimes. Chem Eng Sci. 2018;184:33–51. https://doi.org/10.1016/j.ces.2018.03.038.

Gidaspow D. Multiphase flow and fluidization: continuum and kinetic theory descriptions. Cambridge: Academic press; 1994.

Gidaspow D, Bacelos M. Kinetic theory based multiphase flow with experimental verification. Rev Chem Eng. 2018;34(3):299–318. https://doi.org/10.1515/revce-2016-0044.

Han Q, Yang N, Zhu J, Liu M. Onset velocity of circulating fluidization and particle residence time distribution: a CFD–DEM study. Particuology. 2015;21:187–95. https://doi.org/10.1016/j.partic.2014.10.011.

He Y, Evans T, Shen Y, Yu A, Yang R. Discrete modelling of the compaction of non-spherical particles using a multi-sphere approach. Miner Eng. 2018;117:108–16. https://doi.org/10.1016/j.mineng.2017.12.013.

Hua L, Zhao H, Li J, Wang J, Zhu Q. Eulerian–Eulerian simulation of irregular particles in dense gas–solid fluidized beds. Powder Technol. 2015;284:299–311. https://doi.org/10.1016/j.powtec.2015.06.057.

Huilin L, Gidaspow D. Hydrodynamics of binary fluidization in a riser: CFD simulation using two granular temperatures. Chem Eng Sci. 2003;58(16):3777–92. https://doi.org/10.1016/S0009-2509(03)00238-0.

Igci Y, Pannala S, Benyahia S, Sundaresan S. Validation studies on filtered model equations for gas-particle flows in risers. Ind Eng Chem Res. 2011;51(4):2094–103. https://doi.org/10.1021/ie2007278.

Johnson PC, Nott P, Jackson R. Frictional–collisional equations of motion for participate flows and their application to chutes. J Fluid Mech. 1990;210:501–35. https://doi.org/10.1017/S0022112090001380.

Jung J, Gidaspow D, Gamwo IK. Measurement of two kinds of granular temperatures, stresses, and dispersion in bubbling beds. Ind Eng Chem Res. 2005;44(5):1329–41. https://doi.org/10.1021/ie0496838.

Khawaja HA. Sound waves in fluidized bed using CFD–DEM simulations. Particuology. 2018;38:126–33. https://doi.org/10.1016/j.partic.2017.07.002.

Langston P, Matchett A, Fraige F, Dodds J. Vibration induced flow in hoppers: continuum and DEM model approaches. Granul Matter. 2009;11(2):99–113. https://doi.org/10.1007/s10035-009-0125-7.

Li J. Particle-fluid two-phase flow: the energy-minimization multi-scale method. Beijing: Metallurgical Industry Press; 1994.

Li JJ, Liu Y, Gao YJ, Cheng BY, Jiang HQ. Pore-scale study of the pressure-sensitive effect of sandstone and its influence on multiphase flows. Pet Sci. 2019;16(2):382–95. https://doi.org/10.1007/s12182-018-0266-6.

Lu Y, Wei L, Wei J. A numerical study of bed expansion in supercritical water fluidized bed with a non-spherical particle drag model.

Chem Eng Res Des. 2015;104:164–73. https://doi.org/10.1016/j.cherd.2015.08.005.
Lungu M, Wang H, Wang J, Yang Y, Chen F. Two-fluid model simulations of the national energy technology laboratory bubbling fluidized bed challenge problem. Ind Eng Chem Res. 2016;55(17):5063–77. https://doi.org/10.1021/acs.iecr.5b04511.
Marchelli F, Moliner C, Bosio B, Arato E. A CFD–DEM study of the behaviour of single-solid and binary mixtures in a pyramidal spouted bed. Particuology. 2019;42:79–91. https://doi.org/10.1016/j.partic.2018.03.017.
Mehrabadi M, Murphy E, Subramaniam S. Development of a gas–solid drag law for clustered particles using particle-resolved direct numerical simulation. Chem Eng Sci. 2016;152:199–212. https://doi.org/10.1016/j.ces.2016.06.006.
Miao Z, Zhou Z, Yu A, Shen Y. CFD–DEM simulation of raceway formation in an ironmaking blast furnace. Powder Technol. 2017;314:542–9. https://doi.org/10.1016/j.powtec.2016.11.039.
Pei P, Zhang K, Lu E, Wen D. CFD simulation of bubbling and collapsing characteristics in a gas–solid fluidized bed. Pet Sci. 2009;6(1):69–75. https://doi.org/10.1007/s12182-009-0013-0.
Radl S, Sundaresan S. A drag model for filtered Euler–Lagrange simulations of clustered gas–particle suspensions. Chem Eng Sci. 2014;117:416–25. https://doi.org/10.1016/j.ces.2014.07.011.
Rangarajan D, Shiozawa T, Shen Y, Curtis J, Yu A. Influence of operating parameters on raceway properties in a model blast furnace using a two-fluid model. Ind Eng Chem Res. 2013;53(13):4983–90. https://doi.org/10.1021/ie301936r.
Sakai M, Abe M, Shigeto Y, Mizutani S, Takahashi H, Vire A et al. Verification and validation of a coarse grain model of the DEM in a bubbling fluidized bed. Chem Eng J. 2014;244:33–43. https://doi.org/10.1016/j.cej.2014.01.029.
Sarkar A, Milioli FE, Ozarkar S, Li T, Sun X, Sundaresan S. Filtered sub-grid constitutive models for fluidized gas-particle flows constructed from 3-D simulations. Chem Eng Sci. 2016;152:443–56. https://doi.org/10.1016/j.ces.2016.06.023.
Sharma A, Wang S, Pareek V, Yang H, Zhang D. CFD modeling of mixing/segregation behavior of biomass and biochar particles in a bubbling fluidized bed. Chem Eng Sci. 2014;106:264–74. https://doi.org/10.1016/j.ces.2013.11.019.
Shi JF, Deng F, Xiao LZ, Liu HB, Ma FQ, Wang MY et al. A proposed NMR solution for multi-phase flow fluid detection. Pet Sci. 2019;16(5):1148–58. https://doi.org/10.1007/s12182-019-00367-3.
Sun J, Zhou Y, Ren C, Wang J, Yang Y. CFD simulation and experiments of dynamic parameters in gas–solid fluidized bed. Chem Eng Sci. 2011;66:4972–82. https://doi.org/10.1016/j.ces.2011.06.035.
Syamlal M, Rogers W, OBrien TJ. MFIX documentation theory guide. WV: USDOE Morgantown Energy Technology Center; 1993.
Tenneti S, Garg R, Subramaniam S. Drag law for monodisperse gas–solid systems using particle-resolved direct numerical simulation of flow past fixed assemblies of spheres. Int J Multiph Flow. 2011;37(9):1072–92. https://doi.org/10.1016/j.ijmultiphaseflow.2011.05.010.
Wang Q, Zhang K, Gu H. CFD simulation of pressure fluctuation characteristics in the gas–solid fluidized bed: comparisons with experiments. Pet Sci. 2011;8(2):211–8. https://doi.org/10.1007/s12182-011-0137-x.
Wang ZJ, Tang J, Lu CX. Fluidization characteristics of different sizes of quartz particles in the fluidized bed. Pet Sci. 2016;13(3):584–91. https://doi.org/10.1007/s12182-016-0106-5.
Wen C. Mechanics of fluidization. Chem Eng Prog Symp Ser. 1966;62:100–11.
Wu S, Meng F, He Y. Scale resolution of fiber optical signals in circulating fluidized bed. Chem Eng Sci. 2018;182:162–70. https://doi.org/10.1016/j.ces.2018.02.033.
Yang T, Leu L. Multiresolution analysis on identification and dynamics of clusters in a circulating fluidized bed. AIChE J. 2009;55(3):612–29. https://doi.org/10.1002/aic.11758.
Yan S, He Y, Tang T, Wang T. Drag coefficient prediction for non-spherical particles in dense gas–solid two-phase flow using artificial neural network. Powder Technol. 2019;354:115–24. https://doi.org/10.1016/j.powtec.2019.05.049.
Yang ZL, Yu HY, Chen ZW, Cheng SQ, Su JZ. A compositional model for CO2 flooding including CO2 equilibria between water and oil using the Peng-Robinson equation of state with the Wong-Sandler mixing rule. Pet Sci. 2019;16(4):874–89. https://doi.org/10.1007/s12182-018-0294-2.
Yao J, Zhao Y, Li N, Zheng Y, Hu G, Fan J et al. Mechanism of particle transport in a fully developed wake flow. Ind Eng Chem Res. 2012;51(33):10936–48. https://doi.org/10.1021/ie202749a.
Yin BT, Li XF, Liu G. A mechanistic model of heat transfer for gas–liquid flow in vertical wellbore annuli. Pet Sci. 2018;15(1):135–45. https://doi.org/10.1007/s12182-017-0193-y.
Zhang W. A review of techniques for the process intensification of fluidized bed reactors. Chin J Chem Eng. 2009;17(4):688–702. https://doi.org/10.1016/S1004-9541(08)60264-5.
Zhang Y, Lan X, Gao J. Modeling of gas–solid flow in a CFB riser based on computational particle fluid dynamics. Pet Sci. 2012;9(4):535–43. https://doi.org/10.1007/s12182-012-0240-7.
Zhao Y, Wang Y, Yao J, Fairweather M. Reynolds number dependence of particle resuspension in turbulent duct flows. Chem Eng Sci. 2018;187:33–51. https://doi.org/10.1016/j.ces.2018.04.053.
Zhu HL, Wang SF, Yin GJ, Chen Q, Xu FL, Peng W et al. Study of the numerical simulation of tight sandstone gas molecular diffusion based on digital core technology. Pet Sci. 2018;15(1):68–76. https://doi.org/10.1007/s12182-017-0210-1.
Zhu HP, Zhou ZY, Yang RY, Yu AB. Discrete particle simulation of particulate systems: theoretical developments. Chem Eng Sci. 2007;62(13):3378–96. https://doi.org/10.1016/j.ces.2006.12.089.